Near infrared luminescence of Ba^{2+}/Si^{4+} co-doped$Y_3Ga_5O_{12}$: Cr^{3+} phosphors and their potential applications

Ziman Liu[a], Wanqin Yang[a], Yangyang Zhao[b], Jian Yang[a,] *, Xiaoyu Dong[a], Bohan Lei[a] Hancheng Zhu[a], Duanting Yan[a], Changshan Xu[a] & Yuxue Liu [a,] **

[a] *School of Physics, Northeast Normal University, 5268 Renmin Street, Changchun, 130024, China*

[b] *China-Japan Union Hospital of Jilin University, Changchun 130033, China*

* Corresponding author: E-mail: yangj079@nenu.edu.cn

** Corresponding author: E-mail: yxliu@nenu.edu.cn

Abstract

We synthesized a series of garnet-structured $Y_{3-3y}Ga_{5(1-x)-3y}O_{12}$: xCr^{3+}, yBa^{2+}, ySi^{4+} （x = 0.02, y = 0-0.1） (YGO: Cr^{3+}, yBa^{2+}, ySi^{4+}) near-infrared broadband phosphors via coprecipitation method. Characterization results demonstrated that increasing Ba^{2+}-Si^{4+} doping concentration induced significant particle size growth while maintaining the garnet structure. Under 600 nm excitation, all samples exhibited characteristic Cr^{3+} $^2E \rightarrow {}^4A_2$transition emission centered at 748 nm. Notably, Ba^{2+}- Si^{4+}co-doping produced dual effects: (1) remarkable luminescence enhancement with spectral broadening (FWHM increased from 70 nm to 133 nm), and (2) reduced thermal stability (intensity retention at 413 K decreased from 67% to 57%). To optimize performance, we developed a hybrid system combining thermally stable YGO:Cr^{3+} (x=0.02) with spectrally broadened YGO:Cr^{3+} (x=0.02,y=0.005), which was subsequently integrated with 620 nm red LED chips to fabricate high-performance NIR-I phosphor-converted LEDs. This work not only reveals the fundamental doping effects in garnet phosphors but also provides a practical design strategy for near-infrared luminescent materials.

Key words: Garnet-structured gallate; Near infrared broadband emission; Cr^{3+};

1. Introduction

Near-infrared phosphor-converted light-emitting diodes (NIR pc-LEDs) have

advantages such as small size, long lifespan, low cost, and adjustable spectrum. They play an important role in emerging fields such as food inspection, non-destructive testing, biomedicine, night vision, iris recognition, and information an-ti-counterfeiting[1-4]. When near-infrared light irradiates a sample, the changes in op-tical signals caused by the characteristic absorption or reflection of different wave-lengths of light can be used to analyze intrinsic information about the material. Near-infrared spectroscopy identifies the types of substances based on the characteris-tic absorption of molecular groups, and then uses the distribution of reflected wave-lengths collected by the detector to determine the composition and content of the measured object[5].

The transition metal ion Cr^{3+} has an electronic configuration of [Ar] $3d^3$, with partially filled outermost 3d orbitals. Since the d-d transitions of Cr^{3+} occur within these 3d orbitals, its emission spectrum is highly sensitive to the local coordination environment. Researchers often employ crystal field engineering to manipulate the energy level splitting of Cr^{3+}, thereby tuning both the emission wavelength and spectral bandwidth. [6]Zhao et al. [7]synthesized a series of $KMP_2O_7:Cr^{3+}$ phosphors (M = Ga, Sc, In, and Lu), demonstrating that isovalent cation substitution provides an effective approach to modulate both the host lattice structure and crystal field environment, thereby enabling precise control of luminescence properties. Through systematic variation of the M^{3+} ionic radius (Ga^{3+}: 0.62 Å, Sc^{3+}: 0.745 Å, In^{3+}: 0.80 Å, Lu^{3+}: 0.861 Å), the researchers established clear correlations between local coordination geometry and optical characteristics. Specifically, the progressive expansion of octahedral sites occupied by Cr^{3+} ions with increasing M^{3+} radius leads to a corresponding reduction in crystal field strength, as evidenced by a continuous redshift of the emission maximum from 815 nm (M = Ga) to 900 nm (M = Lu). This structural modification is accompanied by decreased lattice rigidity, which manifests in enhanced electron-phonon coupling through increased Stokes shift and non-radiative transition rates, ultimately resulting in emission bandwidth broadening (FWHM expansion from 125 nm to 178 nm) and reduced thermal stability. Notably, the $KGa_{0.89}P_2O_7:0.11Cr^{3+}$ composition exhibits optimal performance with maximum photoluminescence intensity under 455 nm excitation,

achieving an internal quantum efficiency of 55.8% while maintaining 68% of its room-temperature emission intensity at 423 K. Zeng et al.[8]successfully synthesized $NaInP_2O_7:Cr^{3+}$ phosphors that exhibit broad near-infrared emission under 460 nm blue light excitation. The emission spectrum covers a wide range from 650 to 1150 nm with a characteristic peak centered at 870 nm, demonstrating a full width at half maximum (FWHM) of approximately 150 nm. However, thermal stability measurements revealed that the phosphor maintains only about 20% of its room-temperature emission intensity at 423 K, indicating relatively poor thermal quenching resistance. Yao et al. [9]synthesized $LiScP_2O_7:Cr^{3+}$ phosphors via a high-temperature solid-state reaction method. Under 470 nm excitation, the phosphors exhibited broad near-infrared emission centered at 880 nm with a full width at half maximum (FWHM) of 170 nm. However, thermal stability tests revealed that the material retained only approximately 20% of its initial emission intensity at 423 K, indicating significant thermal quenching behavior. Zou etal.[10] developed an efficient near-infrared phosphor system, H_3BO_3,$Gd_{2.4}Lu_{0.6}Ga_4AlO_{12}:Cr^{3+}$, through strategic optimization of Cr^{3+} octahedral crystal field environment and the incorporation of H_3BO_3 as a flux agent. The phosphor exhibits a broad near-infrared emission band peaking at 728 nm under blue light excitation, with a full width at half maximum (FWHM) of 107 nm that shows excellent spectral matching with the absorption bands of phytochrome far-red (PFR). Remarkably, the material demonstrates superior thermal stability, maintaining 75% of its room-temperature integrated emission intensity at 423 K under 450 nm excitation.

In this work, we synthesized $Y_3Ga_5O_{12}:Cr^{3+}$ phosphors via a co-precipitation method. A series of $Y_{3-3y}Ga_{5(1-x)-3y}O_{12}:xCr^{3+}, yBa^{2+}, ySi^{4+}$（x = 0.02, y = 0-0.1） phosphors were prepared through [Ba^{2+}- Si^{4+}] co-substitution for [Y^{3+}-Ga^{3+}] pairs to modulate Cr^{3+} luminescence. The optimized YGO: $0.02Cr^{3+}$, $0.005Ba^{2+}$, $0.005Si^{4+}$ phosphor was subsequently integrated with a high-efficiency LED chip to fabricate an NIR phosphor-converted LED (pc-LED).

2. Experimental

2.1. Preparation

$C_6H_9O_6Y{\cdot}xH_2O$ (99.99%), $Ga(NO_3)_3$ (99.99%), $Cr(NO_3)_3$ (99.99％), $C_4H_6O_4{\cdot}Ba$ (99%) from Aladdin are dissolved together in distilled water (100ml) according to the composition of $Y_{3-3y}Ga_{5(1-x)-3y}O_{12}$: xCr^{3+}, yBa^{2+}, ySi^{4+}（x = 0.02, y = 0 -0.1） to prepare the mother liquor (0.08mol/L for total concentration).

The as-prepared mother liquor was dropped into $NH_3{\cdot}xH_2O$ (99.99％,1800μl) at a rate of ~200μl/min under magnetic stirring (~690r/min) keeping stirring 2h.Making the resulting white suspension stand for 24 hours. The separated precipitating liquid is centrifuged with distilled water and washed repeatedly to remove impurity ions. The resulting white sediment is dried in an oven at 100℃ for more than 12 hours, and then gently ground with ground platinum to grind the solid into a powder. Finally, the powder is calcined in a furnace at 900 °C for two hours to obtain the desired sample.

2.2 Characterization

The powder samples were characterized by X-ray diffraction (XRD, D/MAX-2500X, Rigaku, Japan). The morphology and elemental composition were analyzed using field emission scanning electron microscopy (SEM, Quanta FEG250, FEI, USA) with energy dispersive X-ray spectroscopy (EDS). The excitation and emission spectra were measured using a Zolix Omin-λ300 spectrofluorometer (Zolix Instruments Co., Ltd, China) equipped with an InGaAs detector (DInGaAs2600-TE). Temperature-dependent emission spectra were collected using the same spectrofluorometer system coupled with an INSTEC HCP621G temperature stage and a 635 nm semiconductor laser (Changchun New Industries Optoelectronics Tech. Co., Ltd). Near-infrared luminescence imaging was performed using a HAMAMATSU C14041-10U InGaAs camera (Hamamatsu Photonics K.K., Japan).

3. Results and discussion

3.1. Structural and Morphological Characterization of YGO:Cr^{3+} (x = 0~0.03) Powder Samples

To investigate the effect of Cr^{3+} doping on the microstructure of the phosphors, X-ray diffraction (XRD) analysis was performed on samples with varying Cr^{3+} concentrations (x = 0, 0.01, 0.015, 0.02, 0.025, and 0.03). As shown in **Fig1.**(a), all diffraction peaks match well with the standard pattern of the $Y_3Ga_5O_{12}$ garnet structure (JCPDS No. 43-0512), and no impurity phases are detected. These results indicate that the partial substitution of Cr^{3+} ions does not alter the host structure, confirming the successful synthesis of pure-phase YGO:xCr^{3+} nanophosphors.

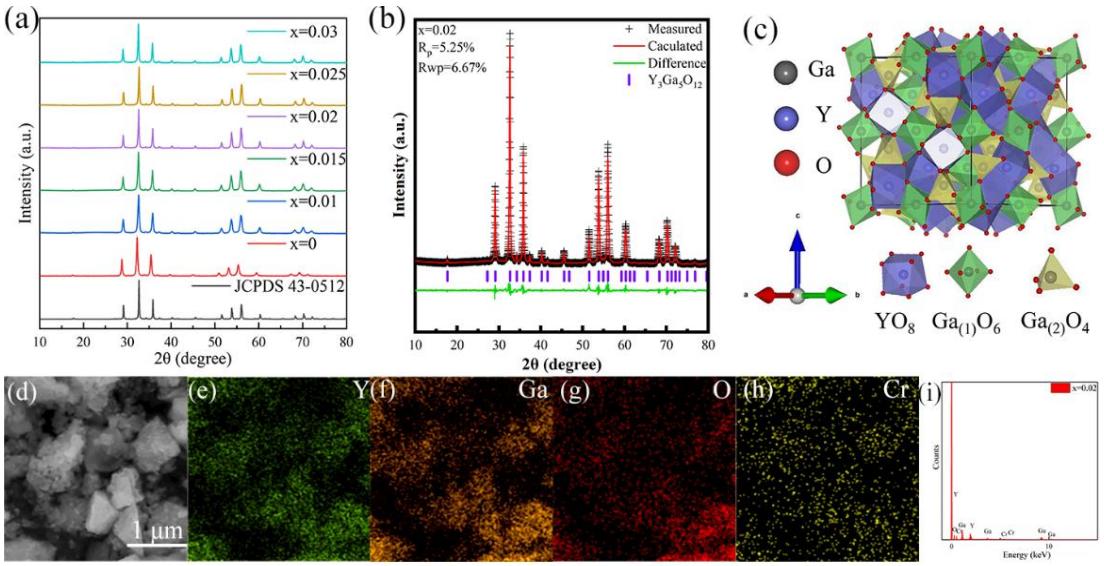

Fig. 1. (a)XRD patterns of YGO:Cr^{3+} powders with different concentrations(x = 0~0.03) (b)Rietveld refinement results of XRD patterns for the YGO:Cr^{3+}(x = 0.02) phosphor; (c)Crystal structure of $Y_3Ga_5O_{12}$;(d)TEM image of a single YGO:Cr^{3+}(x = 0.02) particle and its corresponding (e~h) EDS elemental mapping images; (i)EDS spectrum of YGO:Cr^{3+}(x = 0.02).

To further elucidate the crystal structure of $Y_3Ga_5O_{12}$:Cr^{3+} after Cr^{3+} doping, Rietveld refinement was performed on the XRD pattern of YGO:xCr^{3+} (x = 0.02) nanoparticles. The standard crystal structure of $Y_3Ga_5O_{12}$ (PDF #43-0512) was used as the initial refinement model. As shown in Fig. 1(b), the best-fit refinement of the XRD pattern is presented. The refinement yielded R_{wp} = 6.67% and R_p = 5.25% for the $Y_3Ga_5O_{12}$:Cr^{3+} (x = 0.02) sample, both within reasonable error ranges, confirming the reliability of the refinement results. These satisfactory refinement parameters demonstrate that the YGO:xCr^{3+} nanophosphors maintain the YGO garnet structure, consistent with the

aforementioned XRD analysis.

Fig.1(c) presents the crystal structure of YGO, which adopts a cubic garnet structure with the space group Ia-3d. The cubic lattice parameter was determined to be a = b = c = 1.227390 nm. The figure also illustrates the coordination configurations of ions in this structure. In this garnet framework, Y^{3+} ions occupy the dodecahedral sites (12-coordinated). The Ga^{3+} ions are distributed between two distinct coordination environments: a portion occupies tetrahedral sites with an ionic radius of 0.047 nm, while the remaining Ga^{3+} ions reside in octahedral sites with an ionic radius of 0.062 nm[11]. Compared with Y^{3+} (0.1019 nm), the ionic radius of Cr^{3+} (0.0615 nm) closely matches that of Ga^{3+} occupying octahedral sites (0.062 nm). Therefore, it is reasonable to conclude that in the $Y_3Ga_5O_{12}$ host lattice, Cr^{3+} ions preferentially substitute for octahedrally-coordinated Ga^{3+} ions, which subsequently leads to the observed broad near-infrared emission[12-13].

To further investigate the doping mechanism of Cr^{3+} ions in the YGO garnet structure, we performed first-principles calculations to determine the formation energies of Cr^{3+} substitution at different lattice sites. Since Ga^{3+} ions occupy both octahedral and tetrahedral sites in the YGO structure, we systematically calculated the formation energies for Cr^{3+} substitution at each of these distinct positions. The calculations were carried out using the CASTEP module within the Materials Studio software package. The generalized gradient approximation (GGA) with PW91 functional was employed for all calculations. We constructed a supercell containing 99 atoms of the original $Y_3Ga_5O_{12}$ (abbreviated as YGO, space group Ia-3d, a = b = c = 12.27390 Å, α = β = γ = 90°) to simulate and analyze the YGO system. The following computational parameters were applied[14-15]:

$$\Delta E_f = E_d - E_p - \sum_i n_i \mu_i \quad (1)$$

The formation energy (ΔE_f) is defined as the energy difference between the doped and pristine systems, where E_d and E_p represent the total energies of the unit cell with and without Cr^{3+} doping, respectively. μi represents the chemical potential associated with atom that has been added or removed. The value of ni is +1 (for the added atom)

or − 1 (for removed atom).Our calculations reveal distinct formation energies for Cr^{3+} substitution at different lattice sites: $Ga_{(1)}^{3+}$ octahedral sites ($Ga_{(1)}O_6$): -5.08 eV， $Ga_{(2)}^{3+}$ tetrahedral sites ($Ga_{(2)}O_4$): +10.01 eV. According to solid-state thermodynamics, lower formation energy indicates greater thermodynamic stability and easier synthesis. The significantly negative formation energy (-5.08 eV) for octahedral site substitution strongly suggests that Cr^{3+} ions preferentially incorporate into the $Y_3Ga_5O_{12}$ garnet structure by replacing $Ga_{(1)}^{3+}$ at octahedral sites. This conclusion will be further supported by subsequent analysis of emission spectra and crystal field theory combined with our first-principles calculations. To characterize the morphology and particle size of $Y_3Ga_5O_{12}:Cr^{3+}$ nanomaterials。

To confirm the successful incorporation of Cr^{3+} ions into the YGO:xCr^{3+} nanoparticles, the energy-dispersive X-ray spectroscopy (EDS) spectrum of YGO:xCr^{3+} (x = 0.02) nanophosphors is presented in Fig. 1(i). The characteristic EDS peaks corresponding to Y, Ga, O, and Cr elements are clearly observed. Due to the relatively low Cr content in the YGO:xCr^{3+} nanoparticles, the intensity of Cr signals appears weaker compared to those of the host elements (Y, Ga, and O).Furthermore, the elemental mapping analysis Fig. 1(e-f) demonstrates a homogeneous spatial distribution of Y, Ga, O, and Cr elements within the same region, providing strong evidence for the successful synthesis of phase-pure YGO:xCr^{3+} nanoparticles .For direct morphological observation, the transmission electron microscopy (TEM) image in Fig. 1 (d) reveals that the YGO:xCr^{3+} particles exhibit micron-scale dimensions with well-defined crystalline features.

3.2 Spectral Analysis of YGO:Cr^{3+} (x = 0.01, 0.015, 0.02, 0.025, and 0.03) Phosphors

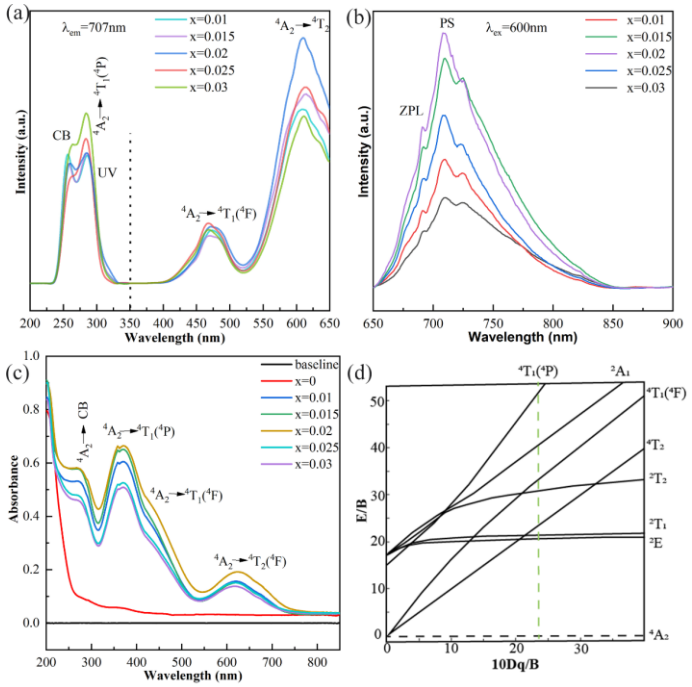

Fig. 2. (a) Excitation spectra(λ_{em} = 707 nm)and (b)emission spectra (λ_{ex} = 600 nm) and of YGO:xCr^{3+} (x = 0.01, 0.015, 0.02,0.025and0.03) nanoparticles. (c) Absorption spectra of YGO:xCr^{3+} (x = 0.01,0.015,0.02,0.025 and 0.03) particles; (d) Tanabe-Sugano energy-level diagram of Cr^{3+} ions in octahedral crystal field.

Fig. 2(a,b) show the normalized PLE and PL spectra of YGO:Cr^{3+}measured at room temperature. **Fig. 1Fig. 2**(a) displays the excitation spectra of $Y_3Ga_{5(1-x)}O_{12}$:xCr^{3+} phosphors with different Cr^{3+} doping concentrations, monitored at 707 nm emission. The excitation spectra of $Y_3Ga_{5(1-x)}O_{12}$:xCr^{3+}(x = 0.01, 0.015, 0.02, 0.025, 0.03) near-infrared persistent luminescence nanoparticles, measured from 220 to 650 nm with emission monitored at 707 nm, consist of four distinct bands with peak positions at 256 nm, 284 nm, 467 nm, and 620 nm. The excitation peak at 256 nm is assigned to the $^4A_2$-conduction band (CB) transition, while the peaks at 284 nm, 467 nm, and 620 nm correspond to the $^4A_2 \rightarrow {}^4T_1(^4P)$, $^4A_2 \rightarrow {}^4T_1(^4F)$, and $^4A_2 \rightarrow {}^4T_2$ transitions of Cr^{3+} ions, respectively, with the most intense excitation observed at 620 nm[16-17]. These spectral characteristics show remarkable similarity to those of octahedrally coordinated Mn^{4+} ions, with the observed differences in excitation peak positions arising from their identical $^3d_3$ electronic configuration in octahedral coordination environments[18-19]. The broad emission

bands unambiguously demonstrate strong electron-phonon coupling during the absorption transitions.

Fig. 2(b) The figure shows the emission spectra of $Y_3Ga_{5(1-x)}O_{12}:xCr^{3+}$ (x = 0.01, 0.015, 0.02, 0.025, 0.03) under 600 nm excitation. As observed in Figure 3-7, excitation at 600 nm produces a broad near-infrared emission band centered at 707 nm (650-900 nm range) with superimposed sharp emission lines. The detailed assignments of these emission peaks will be discussed in subsequent sections. The emission intensity demonstrates a characteristic concentration quenching behavior across the 1-3% doping range, exhibiting a maximum at the optimal 2% Cr^{3+} concentration. This non-monotonic dependence originates from the interplay between two competing factors: (i) below 1% doping, the emission intensity increases proportionally with Cr^{3+} concentration due to the growing number of optically active centers, and (ii) beyond this threshold, the diminished Cr^{3+}-Cr^{3+} separation enables efficient energy migration to quenching sites through dipole-dipole interactions, resulting in enhanced non-radiative relaxation and consequent emission reduction .

To analyze the origin of photoluminescence, Fig. 2(d) presents the Tanabe-Sugano diagram for Cr^{3+} ions with $3d^3$ electronic configuration, showing the relationship between crystal field parameters and energy level positions. The luminescence properties of Cr^{3+} as an activator center are strongly influenced by its local crystal field environment. The analysis reveals that Cr^{3+} in intermediate or strong crystal fields exhibits narrow-band emission near 697 nm, while in weak crystal fields it shows broad near-infrared emission between 650-900 nm. This is exemplified in NIR persistent luminescence materials such as $Gd_3Al_5O_{12}:Cr^{3+}$, $Zn_3Al_2Ge_2O_{10}:Cr^{3+}$, and $Ba_2Mg(BO_3)_2:Cr^{3+}$, where the crystal field parameter $Dq/B > 2.3$ results in narrow emission bands near 700 nm. In NIR persistent luminescence materials such as $Ca_3Ga_2Ge_3O_{10}:Cr^{3+}$ and $Zn_3Ga_2Ge_2O_{10}:Cr^{3+}$, where the crystal field parameter $Dq/B \approx 2.3$, sharp emission peaks are observed near 697 nm. In NIR persistent luminescence materials including $Cd_3Al_2Ge_3O_{12}:Cr^{3+}$ and $CaGdAlO_4:Cr^{3+}$, where the crystal field parameter $Dq/B < 2.3$, broad near-infrared emission bands are observed between 650-900 nm. For Cr^{3+} ions in

crystal fields, the energy positions of the $^4T_2$ and $^4T_1$ states exhibit strong dependence on the Dq/B ratio (where Dq represents the crystal field splitting parameter and B denotes the Racah parameter), while the ^2E and $^2T_1$ energy levels remain essentially unaffected by crystal field variations. Consequently, when Cr^{3+} occupies intermediate or strong crystal field sites, a characteristic narrow emission peak emerges at 688 nm, corresponding to the spin-forbidden $^2E \rightarrow {}^4A_2$ transition. The observation of a distinct narrow emission band at 688 nm in this work strongly suggests that the Cr^{3+} ions occupy strong crystal field sites, where the $^4T_2$ energy level lies above the ^2E level. This interpretation is fully consistent with the Tanabe-Sugano diagram analysis for Cr^{3+} ions in octahedral coordination, which confirms their characteristic $3d^3$ electronic configuration. Under these conditions, the ^2E energy level exhibits minimal dependence on the crystal field strength, while the $^4T_2$ level shows strong field dependence with its energy increasing progressively with enhanced crystal field intensity. According to Grinberg et al., Cr^{3+} ions in strong crystal field environments predominantly emit through the $^2E \rightarrow {}^4A_2$ transition, whereas in weaker crystal fields, the emission primarily occurs via the $^4T_2 \rightarrow {}^4A_2$ transition[22].

In this study, where Cr^{3+} substitutes for Ga^{3+} in $Y_3Ga_5O_{12}$, the absorption spectrum of YGO:Cr^{3+} samples within the 200-800 nm range was measured under octahedral crystal field (O_h) approximation. The spectrum clearly exhibits four characteristic absorption bands centered at 275 nm, 360 nm, 437 nm, and 620 nm. The absorption peak at 275 nm corresponds to the transition from the ground state ($^4A_2$) to the conduction band in Cr^{3+} ions. The absorption bands at 360 nm, 437 nm, and 620 nm are assigned to the $^4A_2 \rightarrow {}^4T_1(^4P)$, $^4A_2 \rightarrow {}^4T_1$ (^4F), and $^4A_2 \rightarrow {}^4T_2(^4F)$ transitions of Cr^{3+} ions, respectively[20]. With increasing Cr^{3+} doping concentration, the absorption intensity enhances while the peak positions remain essentially unchanged, indicating minimal influence of Cr^{3+} concentration variation on the local crystal field environment.

By applying Equations (2) and (3), the crystal field strength parameter (Dq) and Racah parameter (B) can be quantitatively determined[21]:

$$10Dq = E_a(^4T_2) - E_a(^4A_2) \quad (2)$$

$$11Dq + (15/2)Bd = E_a(^4T_1) - E_a(^4A_2) \quad (3)$$

In these equations, Eα represents the energy levels corresponding to the $3d^3$ electronic configuration of Cr^{3+} ions in the excitation spectrum, where $^4A_2$ denotes the ground state, and $^4T_1$ and $^4T_2$ represent excited states. The energy difference between $E_\alpha(^4T_2)$ and $E_\alpha(^4A_2)$ corresponds to the wavenumber (16129 cm^{-1}) of the $^4A_2 \rightarrow {}^4T_2$ absorption peak at 620 nm in the excitation spectrum, yielding 10Dq = 16129 cm^{-1} and thus Dq = 1612.9 cm^{-1}. Similarly, the energy difference between $E_\alpha(^4T_1)$ and $E_\alpha(^4A_2)$ corresponds to the wavenumber (22883 cm^{-1}) of the $^4A_2 \rightarrow {}^4T_1$ absorption peak at 437 nm, giving 11Dq + (15/2)B = 22883 cm^{-1}, from which the Racah parameter B is calculated as 685.48 cm^{-1}. Consequently, the crystal field strength ratio Dq/B = 2.35-2.3 indicates that Cr^{3+} occupies an intermediate crystal field environment, with the ^2E level positioned below the $^4T_2$ level as the first excited state. Struve et al[23]. systematically analyzed various Cr^{3+}-doped garnet phosphors and established a direct correlation between crystal field strength and the ionic radii of host lattice constituents. These findings collectively demonstrate that the broad $^4T_2 \rightarrow {}^4A_2$ emission band spanning 650-950 nm is characteristic of Cr^{3+} ions occupying intermediate-strength crystal field environments.

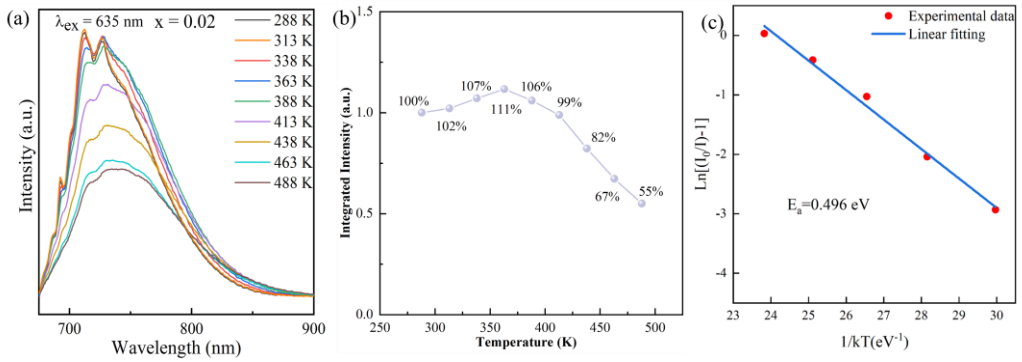

Fig. 3. (a)Temperature-dependent photoluminescence spectra of YGO:Cr^{3+}(x = 0.02)phosphors; (b)The relative luminescence intensity of YGO:Cr^{3+}(x = 0.02) phosphors at different temperatures.(c) The plot of Ln[(I_0/I) − 1] versus 1/kT and the corresponding linear fitting result (red line) using the Arrhenius equation. I_0 and I represent the luminescence intensity at 293 K and the other temperatures, respectively.

To further identify the origin of the narrow emission peaks superimposed on the broadband and to investigate the temperature-dependent luminescence properties of

Cr^{3+}-doped YGO phosphors, **Fig.3**(a) displays the photoluminescence (PL) spectra of the YGO:Cr^{3+} (x = 0.02) powder sample under 635 nm laser excitation at various temperatures. Using a 635 nm red laser as the excitation source, **Fig.3**(b) shows that the luminescence intensity of all YGO:Cr^{3+} phosphors first increases and then decreases with increasing temperature in the range of 288–488 K. The spectra exhibit a strong narrow zero-phonon line (ZPL) emission accompanied by two distinct broad Stokes emission bands. In contrast, the anti-Stokes emission is nearly negligible, which can be attributed to the extremely low phonon density in the lattice, as inferred from the Bose-Einstein distribution law. Interestingly, when the temperature is raised to 313 K, the PL spectra undergo significant changes. Besides the observation that the Stokes emission becomes much stronger than the ZPL emission, the anti-Stokes emission is also markedly enhanced at elevated temperatures. **Fig.3** (c) presents the temperature-dependent integrated emission intensity of YGO:0.02Cr^{3+} phosphors, plotted as $\ln(I_0/I-1)$ versus $T^{-1}\times10^3$ (K^{-1}). To quantitatively analyze the thermal quenching behavior and determine the activation energy for thermal deactivation processes, we employed the Arrhenius equation [28][29]:

$$I(T) = \frac{I_0}{1+Aexp(-\frac{\Delta E}{k_B T})} \tag{4}$$

I_0 represents the integrated emission intensity at the initial maximum peak, ΔE denotes the thermal activation energy for luminescence quenching, and k_B is the Boltzmann constant (1.38×10^{-23} J/K). The thermal activation energy for luminescence quenching in YGO:0.02Cr^{3+}phosphors was determined to be 0.496 eV.

This observation clearly demonstrates that the phonon-assisted vibronic coupling interaction enhances the radiative transition process[24]. The sharp ZPL emission primarily originates from the spin-forbidden transition of $^2E\rightarrow{}^4A_2$, while the broad Stokes emission arises from the spin-allowed radiative transition of $^4T_2\rightarrow{}^4A_2$. Considering ionic radius matching and the lattice coordination environment, Cr^{3+} is generally believed to occupy the Al^{3+} site at the octahedral center in the YAG lattice, exhibiting inversion symmetry[25].

Under these conditions, the ZPL emission of Cr^{3+} occurs exclusively through a

magnetic-dipole (MD) process, primarily due to the identical parity of the ^2E and $^4A_2$ electronic states[26]. This purely electronic transition typically exhibits sharp, narrow, and relatively weak emission intensity. However, localized phonon vibrations may induce slight symmetry distortion in the Cr^{3+} octahedral coordination environment, breaking its inversion symmetry and consequently enabling electric-dipole transitions[27]. Our measurements reveal intense ZPL emission. However, according to the Tanabe-Sugano diagram for d^3 configuration, the Dq/B value of Cr^{3+} in garnet is approximately 2.5, which precisely corresponds to the crossover point between the $^4T_2$ and ^2E states.

These results suggest that the broad Stokes and anti-Stokes emissions likely originate from radiative transitions between the $^4T_2$ and $^4A_2$ vibronic states, corresponding to spin-allowed transition processes. As the temperature increases from 288 K, the vibronic coupling interaction becomes significantly stronger, directly leading to enhanced Stokes and anti-Stokes emissions along with further spectral broadening. However, this enhancement behavior cannot persist at higher temperatures, primarily due to luminescence thermal quenching effects.

Cation substitution provides an effective approach to modulate the octahedral coordination environment of Cr^{3+}. Through synergistic substitution of Ba^{2+} and Si^{4+}, overall charge balance in the lattice can be achieved. The larger ionic radius of Ba^{2+} (0.135 nm, CN=6) substitutes for Y^{3+} (0.09 nm, CN=6), while the smaller Si^{4+} (0.04 nm, CN=6; 0.026 nm, CN=4) replaces Ga^{3+} (0.062 nm), yielding $Y_{3-3y}Ga_{4.9-3y}O_{12}$:0.02$Cr^{3+}$, y$Ba^{2+}$-$Si^{4+}$ ($0.005 \leq y \leq 0.1$) near-infrared phosphors.

This substitution strategy weakens the crystal field strength of the Cr^{3+}-occupied octahedra, resulting in both a red-shifted emission spectrum and broadened FWHM. We systematically investigated the emission spectra, excitation spectra, and thermal stability of the cation-substituted phosphors to elucidate the mechanistic origins of their modified luminescence properties. We fabricated near-infrared pc-LED devices by combining $Y_3Ga_{4.98}O_{12}$:0.02Cr^{3+} and $Y_{2.985}Ga_{4.885}O_{12}$:0.02$Cr^{3+}$,0.005$Si^{4+}$-$Ba^{2+}$ phosphors with red LED chips, and characterized their optoelectronic performance.

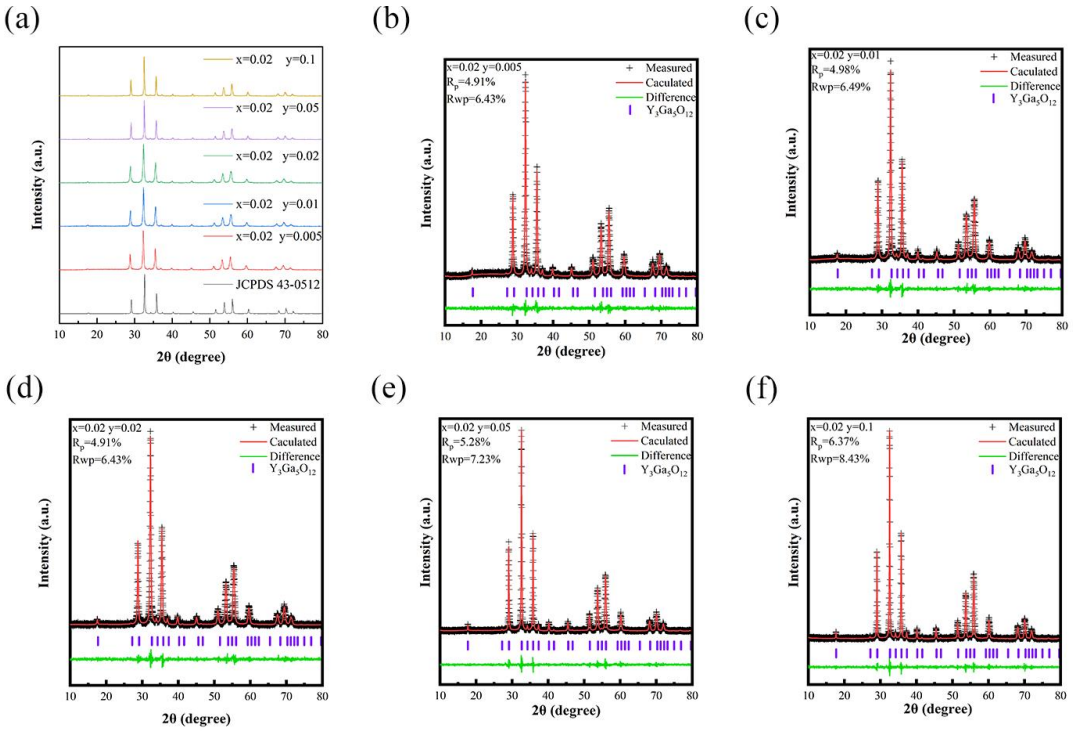

Fig. 4. (a) X-ray diffraction (XRD) patterns of $Y_{3-3y}Ga_{4.9-3y}O_{12}$:0.02$Cr^{3+}$, y$Ba^{2+}$-$Si^{4+}$ ($0.005 \le y \le 0.1$) phosphors. (b)~(f) Rietveld refinement results of XRD data for $Y_{3-3y}Ga_{4.9-3y}O_{12}$:0.02$Cr^{3+}$, y$Ba^{2+}$-$Si^{4+}$ ($0.005 \le y \le 0.1$) phosphors.

Fig. 4(a) shows the X-ray diffraction (XRD) patterns of $Y_{3-3y}Ga_{4.9-3y}O_{12}$:0.02$Cr^{3+}$, y$Ba^{2+}$-$Si^{4+}$ ($0.005 \le y \le 0.1$), where y represents the substitution amount of [Ba^{2+}-Si^{4+}] for [Y^{3+}-Ga^{3+}]. The XRD patterns were collected over a 2θ range of 10° to 80°. As can be seen from **Fig. 4** (a), all diffraction peaks of $Y_{(3-3y)}Ga_{(4.9-3y)}O_{12}$:0.02$Cr^{3+}$, y$Ba^{2+}$-$Si^{4+}$ ($0.005 \le y \le 0.1$) match well with the standard pattern of garnet-type $Y_3Ga_5O_{12}$ (JCPDS No. 43-0512), confirming the successful synthesis of the target products.To obtain detailed structural parameters of $Y_{(3-3y)}$ $Ga_{(4.9-3y)}O_{12}$:0.02Cr^{3+}, yBa^{2+}-Si^{4+} (y = 0~0.1), Rietveld refinement was performed on the XRD patterns using the GSAS software with $Y_3Ga_5O_{12}$ (JCPDS 43-0512) as the initial model. As shown in **Fig. 4**(b)-(f), the refinement results demonstrate good agreement between the experimental and calculated patterns. The obtained reliability factors (R_{wp}, R_p, and χ^2) all fall within acceptable ranges, indicating high data reliability.

The refined structural parameters of $Y_{(3-3y)}Ga_{(4.9-3y)}O_{12}$:0.02$Cr^{3+}$, y$Ba^{2+}$-$Si^{4+}$ (y = 0-0.1) are summarized in **Tab.1**.A gradual increase in unit cell volume was observed with

increasing doping concentration, confirming the successful incorporation of relatively larger Si^{4+} and Ba^{2+} ions into the $Y_3Ga_5O_{12}$ host lattice, which consequently led to lattice expansion.

Tab.1 Rietveld refinement results for the XRD data of $Y_{(3-3y)}Ga_{(4.9-3y)}O_{12}$:0.02$Cr^{3+}$, y$Ba^{2+}$-$Si^{4+}$ (y = 0-0.1) phosphors

x=0.02 y	0.005	0.01	0.02	0.05	0.1
Crystal system	Cubic	Cubic	Cubic	Cubic	Cubic
Space group	Ia-3d	Ia-3d	Ia-3d	Ia-3d	Ia-3d
a(Å)	12.31	12.32	12.37	12.39	12.41
Vol(Å³)	1865.41	1869.96	1892.82	1902	1911.24
R_{wp}	6.43	6.49	6.43	7.23	8.43
X^2	1.059	1.071	1.161	1.175	1.134

Fig.5. shows the scanning electron microscopy (SEM) images of $Y_{(3-3y)}Ga_{(4.9-3y)}O_{12}$:0.02$Cr^{3+}$, y$Ba^{2+}$-$Si^{4+}$ (y = 0-0.1) phosphors, revealing irregularly shaped particles with non-uniform sizes. Significant agglomeration is observed, primarily resulting from the coprecipitation synthesis process.

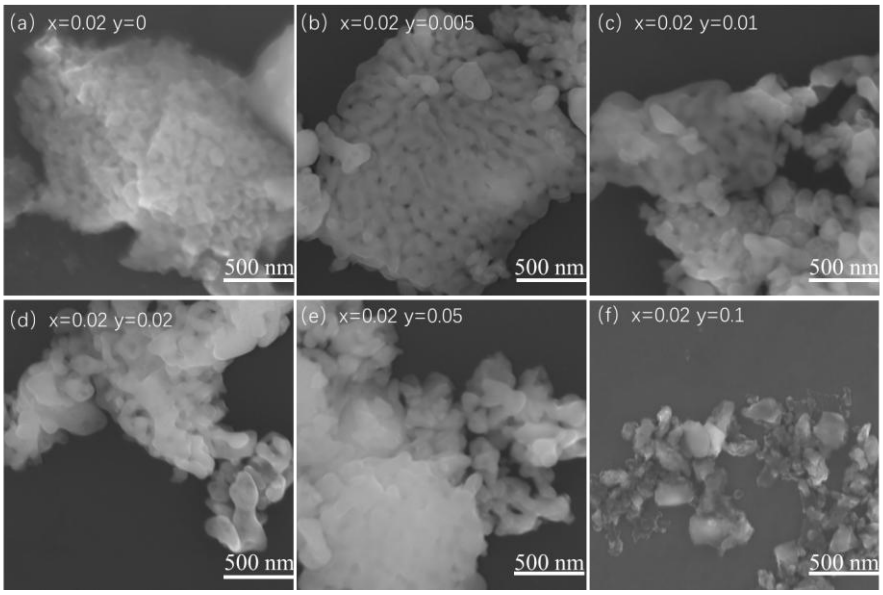

Fig. 5. SEM images of $Y_{(3-3y)}Ga_{(4.9-3y)}O_{12}$:0.02$Cr^{3+}$, y$Ba^{2+}$-$Si^{4+}$ (y = 0-0.1) phosphors.

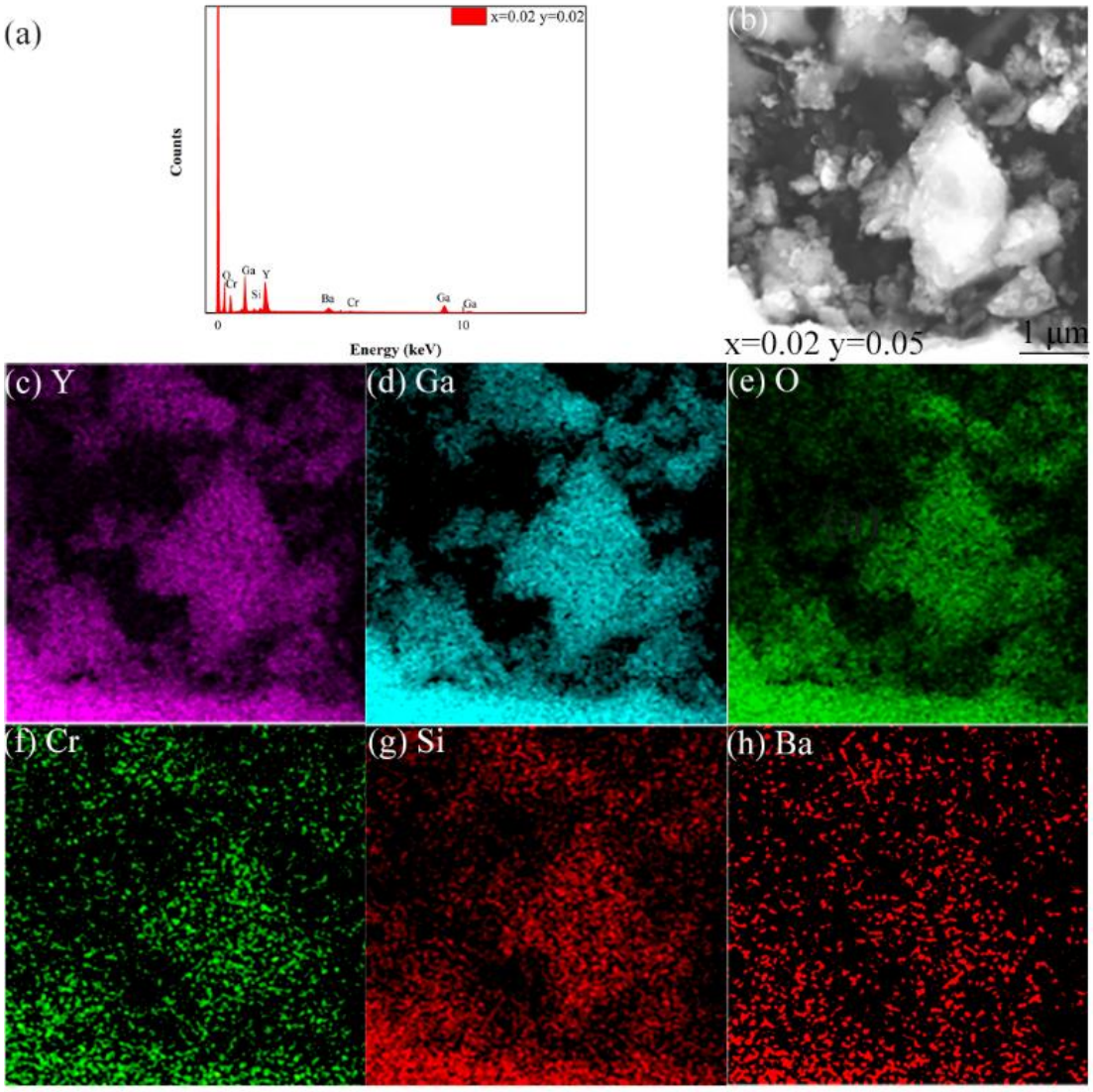

Fig. 6.(a)EDS analysis of $Y_{(3-3y)}Ga_{(4.9-3y)}O_{12}$:0.02$Cr^{3+}$, y$Ba^{2+}$-$Si^{4+}$ (y = 0–0.1) phosphors. TEM image of a single particle of $Y_{(3-3y)}Ga_{(4.9-3y)}O_{12}$:0.02$Cr^{3+}$, y$Ba^{2+}$-$Si^{4+}$ (y = 0–0.1) (b) and the corresponding elemental mapping((c)-(h))

Fig.6.(a) displays the EDS elemental mapping of $Y_{(3-3y)}Ga_{(4.9-3y)}O_{12}$:0.02$Cr^{3+}$, y$Ba^{2+}$-$Si^{4+}$ (y = 0-0.1) phosphors, confirming the homogeneous distribution of Y, Ba, Ga, Si, O, and Cr elements throughout the particles, which further verifies the successful synthesis of the target phosphor. **Fig.6.** (b) shows the TEM image of a single particle, with corresponding EDS elemental mapping results presented in **Fig.6**(c)-(h). The measurements demonstrate uniform distribution of Y, Ba, Ga, Si, O, and Cr elements in the YGO:Cr^{3+} phosphor.

The excitation and emission spectra of $Y_{(3-3y)}Ga_{(4.9-3y)}O_{12}$:0.02$Cr^{3+}$, y$Ba^{2+}$-$Si^{4+}$ (y = 0–0.1) phosphors at room temperature are shown in **Fig.7**(a). Under a detection wavelength of 707 nm, the excitation peaks at 256, 284, 467, and 620 nm are assigned to the $^4A_2$→conduction band (CB), $^4A_2$→$^4T_1$(^4P) transition of Cr^{3+}, $^4A_2$→$^4T_1$(^4F) transition of Cr^{3+}, and the dominant peak at 620 nm to the $^4A_2$→$^4T_2$ transition of Cr^{3+}, respectively. Upon 600 nm excitation, the phosphors emit a broad band (650–900 nm), attributed to the ^2E→$^4A_2$ transition of Cr^{3+}. Notably, YGO:Cr^{3+} exhibits an emission peak at 707 nm with a full width at half maximum (FWHM) of ~70 nm. The short emission wavelength and narrow FWHM restrict its practical applications, demanding further optimization of Cr^{3+} luminescence. Thus, [Ba^{2+}-Si^{4+}] co-substitution for [Y^{3+}–Ga^{3+}] in $Y_3Ga_5O_{12}$ was employed to modify the Cr^{3+}-occupied octahedral environment and tune its emission.

The emission spectra of $Y_{(3-3y)}Ga_{(4.9-3y)}O_{12}$:0.02$Cr^{3+}$, y$Ba^{2+}$-$Si^{4+}$ (y = 0–0.1) phosphors are shown in **Fig.7**(b). Under 600 nm excitation, all samples exhibit broad near-infrared emission in the range of 650–875 nm. For y = 0, the strongest emission peak is located at 707 nm. With increasing [Ba^{2+}-Si^{4+}] doping concentration, the emission profile gradually shifts from a narrow-band emission (peaked at 707 nm) to a broad-band emission (peaked at 748 nm). As seen in **Fig.7** (c), the full width at half maximum (FWHM) of the emission spectra increases from 70 nm to 133 nm as y rises from 0 to 0.1. Additionally, **Fig.7**(c) reveals that the emission intensity initially increases with [Ba^{2+}-Si^{4+}] doping, reaching a maximum at y = 0.005, where the intensity is 1.88 times higher than that of y = 0. This enhancement is attributed to the increased unit cell volume induced by [Ba^{2+}-Si^{4+}] incorporation. However, further doping (y > 0.005) leads to a gradual decrease in emission intensity.

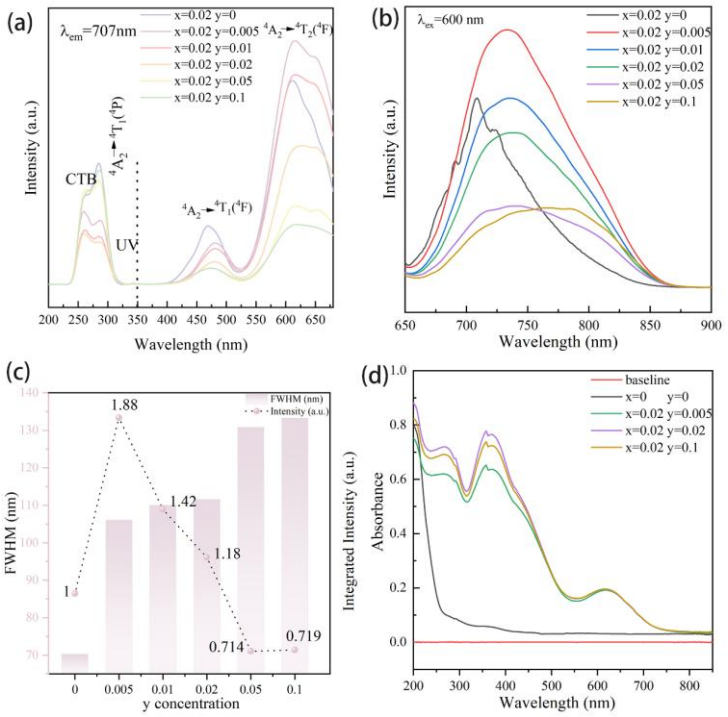

Fig. 7. (a)-(b) Excitation and emission spectra of $Y_{(3-3y)}Ga_{(4.9-3y)}O_{12}$:0.02$Cr^{3+}$, y Ba^{2+}-Si^{4+} (y = 0-0.1) phosphors measured at room temperature. (c) Full width at half maximum (FWHM) and relative emission intensity (normalized to y=0 sample) of $Y_{(3-3y)}Ga_{(4.9-3y)}O_{12}$:0.02$Cr^{3+}$, y$Ba^{2+}$-$Si^{4+}$ (y = 0-0.1) phosphors as a function of doping concentration.

To quantitatively analyze the influence of [Ba^{2+}-Si^{4+}] co-substitution on crystal field strength, the ratio of the crystal field splitting parameter (Dq) to the Racah parameter (B) was employed. The values of Dq and B were determined using the following equations:

$$10Dq = E_\alpha(^4T_2) - E_\alpha(^4A_2) \quad (5)$$

$$11Dq + (15/2)Bd = E_\alpha(^4T_1) - E_\alpha(^4A_2) \quad (6)$$

Dq represents the crystal field splitting parameter, B corresponds to the Racah parameter, and E($^4T_1$) and E($^4T_2$) denote the respective energy level positions of the $^4T_1$ and $^4T_2$ states, as determined from the peak positions in the absorption spectrum **Fig.7** (c).

The crystal field parameters for YGO:0.02Cr^{3+},0.005 Ba^{2+}-Si^{4+} were determined through spectroscopic analysis of the characteristic absorption peaks. The $^4A_2 \rightarrow {}^4T_2$ transition observed at 615 nm (16260 cm^{-1}) yields a crystal field splitting parameter of

Dq = 1626 cm^{-1} through the relationship 10Dq = E($^4T_2$)-E($^4A_2$) = 16260 cm^{-1}. Furthermore, analysis of the $^4A_2 \rightarrow {}^4T_1$ transition at 425 nm (23529 cm^{-1}) using the equation 11Dq + (15/2)B = 23529 cm^{-1} gives a Racah parameter B = 752.4 cm^{-1}. These derived parameters (Dq = 1626 cm^{-1}, B = 752.4 cm^{-1}) provide the fundamental basis for evaluating the crystal field strength through the Dq/B ratio of 2.16<2.35. The [Ba^{2+}-Si^{4+}] co-doping in YGO:Cr^{3+} induces a systematic reduction in crystal field strength, as evidenced by the decrease in Dq/B ratio from 2.35 (undoped) to 2.16 (co-doped). This crystal field modification triggers a fundamental shift in the Cr^{3+} emission mechanism: in the strong-field regime (Dq/B > 2.3), the $^2E \rightarrow {}^4A_2$ transition dominates, yielding narrow-band emission (λ_{em} = 707 nm, FWHM = 70 nm); whereas in the weakened field (Dq/B = 2.16), the $^4T_2 \rightarrow {}^4A_2$ transition becomes predominant, producing broad-band emission (λ_{em} = 748 nm, FWHM = 133 nm). The reduced crystal field strength lowers both the $^4T_1$ and $^4T_2$ energy levels while increasing the thermal population of the $^4T_2$ state from ^2E, resulting in the observed 41 nm red-shift and 90% broadening of the emission band. These findings demonstrate that [Ba^{2+}-Si^{4+}] co-substitution provides an effective approach for tuning Cr^{3+} luminescence through precise control of the local crystal field environment.

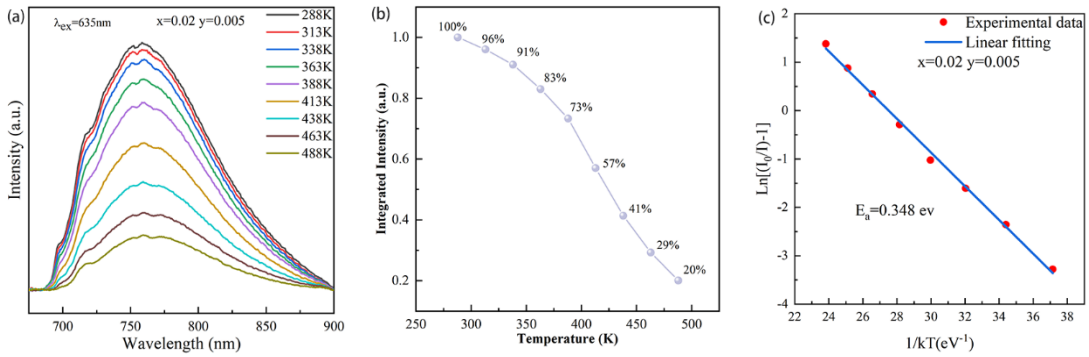

Fig. 8. (a) Temperature-dependent photoluminescence spectra of YGO:0.02Cr^{3+}, 0.005Ba^{2+}-Si^{4+}phosphors. (b) Relative emission intensity (normalized to 288 K) of YGO:0.02Cr^{3+}, 0.005Ba^{2+}-Si^{4+} phosphor as a function of temperature. (c) The plot of Ln[(I_0/I) − 1] versus 1/kT and the corresponding linear fitting result (red line) using the Arrhenius equation. I_0 and I represent the luminescence intensity at 293 K and the other temperatures, respectively.

The temperature-dependent luminescence properties of YGO:0.02Cr^{3+},0.005Ba^{2+}-Si^{4+} phosphors reveal important insights into their thermal stability and emission mechanisms. Under 635 nm excitation, the phosphors exhibit characteristic broadband emission from 288 K to 488 K, as shown in Fig. 8 (a). Three key observations emerge from this study:

First, the integrated emission intensity shows a gradual thermal quenching behavior while maintaining spectral integrity, with less than 5% variation in full width at half maximum. This stability stems from the robust intermediate crystal field environment (Dq/B≈2.16) created by [Ba^{2+}-Si^{4+}] co-doping, where the $^4T_2$ state remains the lowest excited level, favoring the spin-allowed $^4T_2 \rightarrow {}^4A_2$ transition.

Second, the thermal quenching mechanism involves competing processes: (i) thermal energy progressively populates non-radiative decay channels, particularly above 450 K where non-radiative rates exceed radiative transitions by an order of magnitude; (ii) temperature-induced crystal field fluctuations enhance electron-phonon coupling; and (iii) gradual thermal dissociation of Cr^{3+} centers occurs at the highest temperatures.

Third, the preserved spectral profile suggests that the basic electronic structure remains intact across this temperature range, though the weakened crystal field increases sensitivity to thermal perturbations. These findings highlight both the potential and limitations of this material system - while the co-doping approach successfully engineers the emission characteristics, the thermal stability above 450 K requires further improvement for practical applications.

This systematic investigation provides fundamental understanding of the structure-property relationships in these modified garnet phosphors, offering guidance for future materials optimization.

Fig. 8 (c) presents the temperature-dependent integrated emission intensity of YGO:0.02Cr^{3+},0.005Ba^{2+}-Si^{4+} phosphors, plotted as $\ln(I_0/I-1)$ versus $T^{-1}\times10^3$ (K^{-1}). To quantitatively analyze the thermal quenching behavior and determine the activation energy for thermal deactivation processes, we employed the Arrhenius equation [28-29]:

$$I(T) = \frac{I_0}{1+Aexp(-\frac{\Delta E}{k_B T})} \quad (7)$$

I_0 represents the integrated emission intensity at the initial maximum peak, ΔE denotes the thermal activation energy for luminescence quenching, and k_B is the Boltzmann constant (1.38×10^{-23} J/K). The thermal activation energy for luminescence quenching in YGO:$0.02Cr^{3+}$,$0.005Ba^{2+}$-Si^{4+} phosphors was determined to be 348 meV. **Fig. 8**(b) displays the temperature-dependent emission intensity retention ratio relative to the 288 K reference. At the optimal doping concentration (y = 0.005), the phosphor maintains 57% of its initial emission intensity at 413 K, demonstrating reduced thermal stability compared to singly-doped samples.

To develop phosphor-converted LEDs (PC-LEDs) with enhanced luminescence intensity, broadened emission bandwidth, and improved thermal stability, we systematically investigated mixed phosphor systems comprising $Y_{2.985}Ga_{4.885}O_{12}$:$0.02Cr^{3+}$ and $Y_{2.985}Ga_{4.885}O_{12}$:$0.02Cr^{3+}$,$0.005Ba^{2+}$-$Si^{4+}$ at varying mass ratios (0-0.8). As shown in Figure 9a, all mixed samples exhibited spectral broadening compared to the single phosphor, with the 0.8 ratio mixture demonstrating maximum emission intensity at room temperature. Remarkably, this optimal composition (0.8 ratio) also displayed the best thermal stability (Figure 9b), as evidenced by its superior integrated intensity retention at elevated temperatures, making it particularly promising for high-performance PC-LED applications.

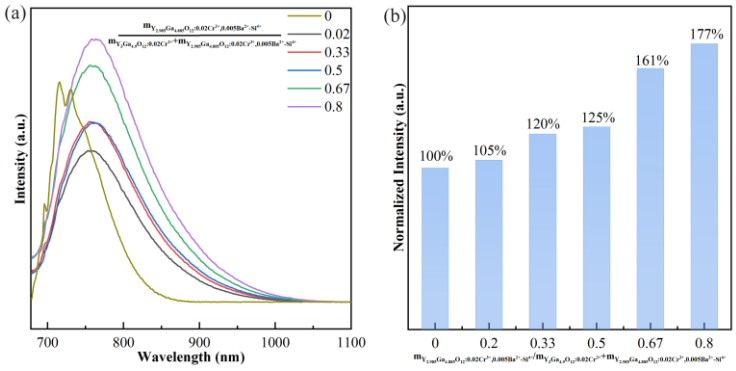

Fig. 9. (a) Photoluminescence (PL) spectra of $Y_3Ga_{4.98}O_{12}$:$0.02Cr^{3+}$ phosphor and a mixed powder of $Y_{2.985}Ga_{4.885}O_{12}$:$0.02Cr^{3+}$, $0.005Ba^{2+}$-Si^{4+} (in a defined ratio) under 635 nm laser excitation at room temperature. (b) Integrated intensity ratio at 413 K between the mixed powder ($Y_{2.985}Ga_{4.885}O_{12}$:$0.02Cr^{3+}$, $0.005Ba^{2+}$-Si^{4+}) and the reference $Y_{2.985}Ga_{4.885}O_{12}$:$0.02Cr^{3+}$ phosphor.

4. Applications of YGO:Cr^{3+} Phosphors

4.1 Fabrication of NIR-I pc-LEDs

Fig. 10. (a) illustrates the fabrication process of NIR-I pc-LEDs. The encapsulation procedure began with preparing a silicone matrix by thoroughly mixing LED encapsulation silicone Parts A and B at a 1:4 mass ratio. Subsequently, 0.0500 g of YGO:0.02Cr^{3+} NIR-I phosphor and 0.0500 g of an optimized phosphor mixture (YGO:0.02Cr^{3+},0.005Ba^{2+}-Si^{4+}:YGO:0.02Cr^{3+} = 0.8:0.2 mass ratio) were separately blended with 0.0500 g of the prepared silicone resin. Each mixture was stirred clockwise to achieve homogeneous dispersion, followed by 2 h degassing. Based on the excitation spectra showing strong broadband excitation at 610 nm for both phosphor systems, a 620 nm red LED chip was selected as the excitation source. The phosphor-silicone composites were then dispensed onto the chips and thermally cured through a two-stage process (90 °C for 1 h followed by 150 °C for 4 h) to complete the pc-LED packaging. As shown in Figure 10(b), the 620 nm LED chip was employed as the excitation source due to its spectral matching with the phosphors' excitation characteristics.

Fig. 10. (b)-(d) present optical images of: (b) a 620 nm red LED chip (3V, 1W), (c) the LED chip with centrally encapsulated YGO:0.02Cr^{3+} NIR-I phosphor, and (d) the pc-LED containing the optimized phosphor mixture (YGO:0.02Cr^{3+},0.005Ba^{2+}-Si^{4+}:YGO:0.02Cr^{3+} = 0.8:0.2) in their unpowered states. The images clearly demonstrate complete curing of the phosphor-silicone composite on the chip surfaces, showing uniform distribution and good adhesion of the phosphor materials.**Fig. 10. (e)-(g)** show photographs of powered devices captured using a conventional digital camera: (e) the bare 620 nm LED chip, (f) the LED with centrally encapsulated YGO:0.02Cr^{3+} phosphor, and (g) the device containing the optimized 0.8:0.2 mixed phosphor system (YGO:0.02Cr^{3+},0.005Ba^{2+}-Si^{4+}:YGO:0.02Cr^{3+}). All three configurations exhibit bright red emission, with a characteristic yellowish-white overexposure zone at the center caused by the intense light output from the LED chip that exceeds the camera's dynamic range. To further characterize the emission wavelength of the LED chip, the inset in **Fig. 10**.(e) presents its electroluminescence spectrum when powered. The spectral

analysis reveals a single emission peak centered at approximately 620 nm, demonstrating the monochromatic nature of the chip's output.

Fig. 10(h)-(j) present near-infrared images acquired using an InGaAs camera for three powered configurations: (h) the bare LED chip, (i) the device with centrally encapsulated YGO:0.02Cr^{3+} phosphor, and (j) the pc-LED containing the optimized 0.8:0.2 mixed phosphor system (YGO:0.02Cr^{3+},0.005Ba^{2+}-Si^{4+}:YGO:0.02Cr^{3+}). In **Fig. 10**(i)-(j)**,** the NIR-I emission signals from both pc-LED configurations are clearly captured by the InGaAs near-infrared camera, exhibiting perfect spectral consistency with the corresponding phosphor samples' characteristic emission profiles. Furthermore, the insets in **Fig. 10**(i)-(j) demonstrate that the InGaAs near-infrared camera precisely captures the NIR emission from pc-LEDs with centrally encapsulated phosphors, showing complete spectral agreement with the reference powder samples. Comparative analysis between the two configurations clearly demonstrates that the pc-LED incorporating the optimized 0.8 mass ratio phosphor mixture (YGO:0.02Cr^{3+},0.005Ba^{2+}-Si^{4+}:YGO:0.02Cr^{3+}) exhibits significantly stronger NIR-I emission intensity. Our experimental results confirm that this specially formulated phosphor system delivers exceptional near-infrared performance.

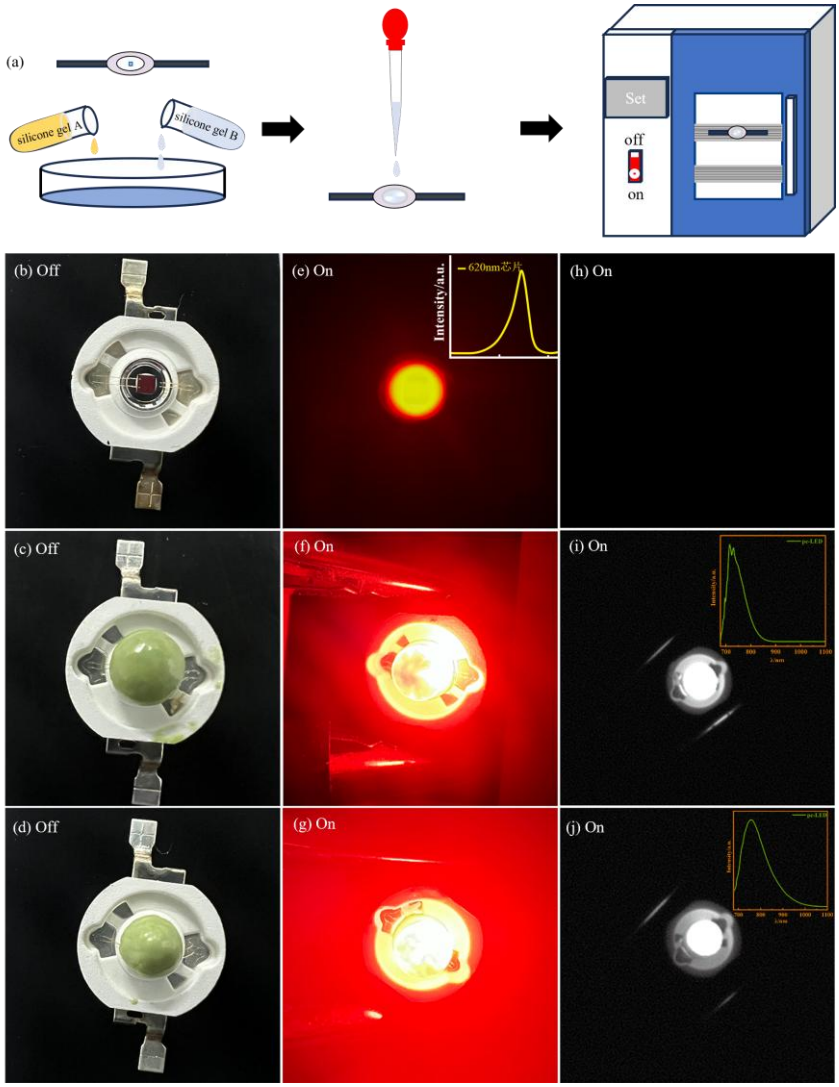

Fig. 10. (a) Fabrication flowchart of NIR-I pc-LEDs; (b)-(g) Photographic images captured by a conventional camera showing: (b) a 620 nm red LED chip, (c) the luminescent area encapsulated with YGO:0.02Cr^{3+} NIR-I phosphor in unpowered state, (d) the same in powered state, (e) the mixed phosphor pc-LED (YGO:0.02Cr^{3+},0.005Ba^{2+}-Si^{4+}:YGO:0.02Cr^{3+} = 0.8:0.2) in unpowered state, (f) powered state, with the inset in (e) displaying the visible-range emission spectrum of the LED chip; (h)-(j) NIR images captured by an InGaAs camera showing: (h) the powered LED chip, (i) the YGO:0.02Cr^{3+} phosphor-encapsulated device, and (j) the mixed phosphor pc-LED, with insets presenting their respective NIR-I range emission spectra.

4.2 Potential Applications of NIR pc-LEDs

To evaluate the practical performance of our optimized NIR-I pc-LED

(YGO:0.02Cr^{3+},0.005Ba^{2+}-Si^{4+}:YGO:0.02Cr^{3+} = 0.8:0.2), we conducted tissue penetration imaging experiments as demonstrated in Figure 11. The device successfully achieved high-contrast venous imaging through 20 mm-thick human finger tissue under complete darkness, with the infrared camera clearly resolving subcutaneous venous structures.

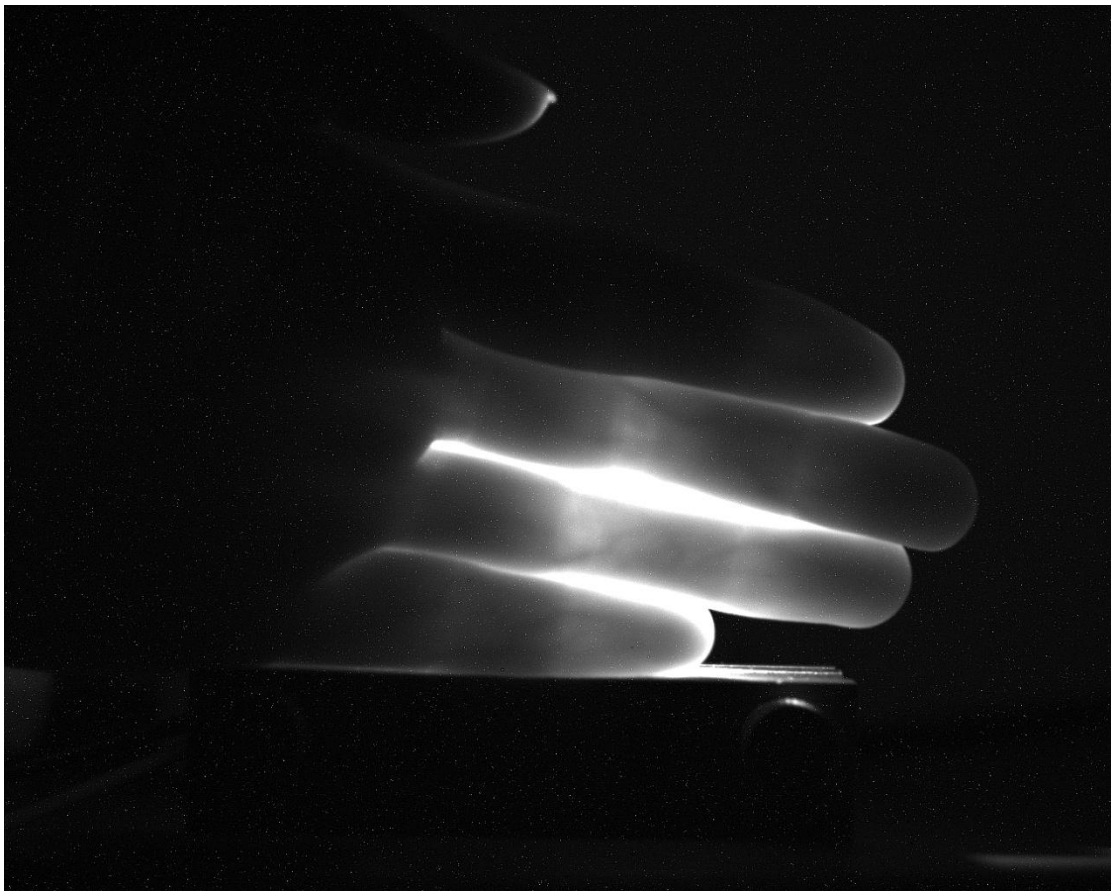

Fig. 11. demonstrates the tissue penetration capability of our NIR-I pc-LED through near-infrared imaging of a human hand under complete darkness.

5. Conclusions

This work reports the successful preparation of $Y_{(3-3y)}Ga_{(4.9-3y)}O_{12}$:0.02$Cr^{3+}$, y$Ba^{2+}$-$Si^{4+}$ (y = 0-0.1) micron-sized phosphors with broadband NIR-I emission via a coprecipitation method, with systematic investigation of Ba^{2+}-Si^{4+} doping effects on morphological and optical properties. The results demonstrate that while increasing Ba^{2+}-Si^{4+} doping concentration leads to gradual particle size enlargement and generally reduced NIR-I emission intensity at ~748 nm, an optimal doping level (y=0.005) exhibits enhanced luminescence intensity and broadened FWHM compared to undoped YGO:Cr^{3+},

attributed to the increased particle size. However, temperature-dependent spectral analysis revealed compromised thermal stability in the y=0.005 sample. To balance these properties, we developed an NIR-I pc-LED by combining the optimal-FWHM phosphor (y=0.005) with the best thermal-stability single-doped phosphor (y=0) on a red LED chip. This pc-LED enabled clear visualization of finger vein patterns when used as an illumination source with an NIR camera, demonstrating the potential of NIR-I pc-LED technology for developing non-invasive, low-cost, and compact medical imaging systems. The study provides important insights into phosphor engineering while establishing a practical approach for next-generation biomedical imaging applications.

Acknowledgements

This work was supported by the Jilin Provincial Scientific and Technological Development Program (Grant No. 20250102015JC), the National Natural Science Foundation of China (Grant No. 12374391, 12204093, U25A20195 and 12074062) and China-Japan Union Hospital of Jilin University MED+X Interdisciplinary Discipline Cultivation Program (Grant No. 2025010).

Author Contributions

Ziman Liu: Writing-original draft, Methodology, Investigation, Formal analysis.

Jian Yang: Writing review & editing, Conceptualization, Supervision, Formal analysis.

Yuxue Liu: Supervision, Resources, Conceptualization.

Reference

[1] A.A. Lucero, G. Addae, W. Lawrence, B. Neway, D.P. Credeur, J. Faulkner, D. Rowlands, L. Stoner, Reliability of muscle blood flow and oxygen consumption response from exercise using near-Infrared spectroscopy. Exp. Physiol. 103 (2018) 90–100.

[2] D. Liu, G. Li, P. Dang, Q. Zhang, Y. Wei, L. Qiu, H. Lian, M. Shang, J. Lin, Valence conversion and site reconstruction in near-infrared-emitting chromium-activated garnet for simultaneous enhancement of quantum efficiency and thermal stability, Light Sci. Appl. 12 (2023) 248.

[3] H. Yu, J. Yang, Y.G. Liu, C. Xie, Z. Huang, L. Mei, Green HF-Free synthetic route to the high-efficiency $K_2NaGaF_6:Cr^{3+}$ phosphor and its NIR-LED application toward veins imaging, ACS Sustain. Chem. Eng. 10 (2022) 8022–8030.

[4] C. Wang, X. Wang, Y. Zhou, S. Zhang, C. Li, D. Hu, L. Xu, H. Jiao, An ultrabroadband near-infrared Cr^{3+}-Activated gallogermanate $Mg_3Ga_2GeO_8$

phosphor as light sources for food analysis, ACS Appl. Electron. Mater. 1 (2019) 1046–1053

[5] Wang C, Wang X, Zhou Y, et al. An Ultra-Broadband Near-Infrared Cr^{3+} -Activated Gallogermanate $Mg_3Ga_2GeO_8$ Phosphor as Light Sources for Food Analysis[J]. ACS Applied Electronic Materials, 2019, 1(6): 1046-1053

[6] Zhao F, Song Z, Liu Q. Advances in Chromium-Activated Phosphors for Near-Infrared Light Sources [J]. Laser & Photonics Reviews, 2022, 16(11): 2200380.

[7] Zhao F Y, Cai H, Zhang S Y, et al. Octahedron-dependent near-infrared luminescence in Cr^{3+} -activated phosphors[J]. Materials Today Chemistry, 2022, 23.

[8] Zeng L, Zhong J, Li C, et al. Broadband near-infrared emission in the $NaInP_2O_7:Cr^{3+}$ phosphor for light-emitting-diode applications[J]. Journal of Luminescence, 2022, 247.

[9] Yao L, Shao Q, Han S, et al. Enhancing Near-Infrared Photoluminescence Intensity and Spectral Properties in Yb^{3+} Codoped $LiScP_2O_7:Cr^{3+}$[J]. Chemistry of Materials, 2020, 32(6): 2430-2439.

[10] Zou X, Wang X, Zhang H, et al. A highly efficient and suitable spectral profile Cr^{3+} - doped garnet near-infrared emitting phosphor for regulating photomorphogenesis of plants[J]. Chemical Engineering Journal, 2022, 428.

[11] Shannon R D. Revised effective ionic radii and systematic studies of interatomic distances in halides and chalcogenides[J]. Foundations of Crystallography, 1976, 32(5): 751-767.

[12] J. Xu, J. Ueda, Y. Zhuang, B. Viana, S. Tanabe, $Y_3Al_{5x}Ga_xO_{12}$: Cr^{3+}: a novel red persistent phosphor with high brightness, Appl. Phys. Express 8 (4) (2015), 042602

[13] J. Ueda, P. Dorenbos, A.J.J. Bos, K. Kuroishi, S. Tanabe, Control of electron transfer between Ce^{3+} and Cr^{3+} in the $Y_3Al_{5-x}Ga_xO_{12}$ host via conduction band engineering, J. Mater. Chem. C 3 (22) (2015) 5642–5651.

[14] Xiang J, Zhou X, Zhao X, et al. Ab initio site-selective occupancy and luminescence enhancement in broadband NIR emitting phosphor $Mg_7Ga_2GeO_{12}:Cr^{3+}$ [J]. Laser & Photonics Reviews, 2023, 17(7): 2200965.

[15] Li C, Ding S, Song T, et al. Structure and microwave dielectric properties of $BaAl_{2-2x}Li_{2x}Si_2O_{8-2x}$ ceramics [J]. Ceramics International, 2021, 47(4): 4895-4904.

[16] Y. Honda, S. Motokoshi, T. Jitsuno, K. Fujioka, M. Nakatsuka, M. Yoshida, T. Yamada, J. Kawanaka, N. Miyanaga, Temperature-dependent fluorescence decay and energy transfer in Nd/Cr:YAG ceramics, Opt. Mater. 90 (2019) 215–219.

[17] T. Xu, L. Yuan, Y. Chen, Y. Zhao, L. Ding, J.M. Liu, W.D. Xiang, X.J. Liang, $Y_3Al_5O_{12}:Ce^{3+}$ single crystal and red-emitting $Y_3Al_5O_{12}:Cr^{3+}$ single crystal for high power W-LEDs, Opt. Mater. 91 (2019) 30–34.

[18] L.Z. Zhang, Y. Yang, F. Tang, S.J. Xu, Z.H. Wang, C.C. Zheng, J.Q. Ning, K.Z. Tian, Luminescence performance and vibronic behavior of Mn4+-activated $Ca_{14-x}K_xAl_{10}Zn_6O_{35}$ deep-red phosphor, Opt. Lett. 46 (2021) 235938–235941.

[19] D.B. Zhang, Y.R. Zheng, K.C. Lu, Z.H. Wang, F. Tang, J.Q. Ning, S.J. Xu, C. C. Zheng, Temperature-dependent electroluminescence of phosphor-converted white LEDs with $K_2SiF_6:Mn^{4+}$ below room temperature, IEEE Electron. Device Lett. 43

(2022) 3151117–3151120.
[20] Chen D, Wan Z, Zhou Y, et al. Dual-phase glass ceramic: structure, dual-modal luminescence, and temperature sensing behaviors[J]. ACS Appl Mater Interfaces. 2015,7(34): 19484-19493.
[21] Xu D, Qiu Z, Zhang Q, et al. Sr_2MgWO_6: Cr^{3+} phosphors with effective near-infrared fluorescence and long-lasting phosphorescence[J]. Journal of Alloys and Compounds. 2019,781: 473-478.
[22] Pratapkumar C, Prashantha S C, Nagabhushana H, et al. Photoluminescence and photometric studies of low temperature prepared red emitting $MgAl_2O_4$: Cr^{3+} nanophosphors for solid state displays[J]. Journal of Science: Advanced Materials and Devices. 2018,3(4): 464-470.
[23] B. Struve, G. Huber, The effect of the crystal field strength on the optical spectra of Cr^{3+} in gallium garnet laser crystals, Appl. Phys. B 36 (4) (1985) 195–201.
[24] Z.C. Su, Z.Y. Ren, Y.T. Bao, X.Z. Lao, J.F. Zhang, J.C. Zhang, D.L. Zhu, Y.M. Lu, Y. Hao, S.J. Xu, Luminescence landscapes of nitrogen-vacancy centers in diamond: quasi-localized vibrational resonances and selective coupling, J. Mater. Chem. C 7 (2019) 8086–8091.
[25] P. Gluchowski, R. Pazik, D. Hreniak, W. Strek, Luminescence properties of Cr^{3+}: $Y_3Al_5O_{12}$ nanocrystals, J. Lumin. 129 (2009) 548–553.
[26] M. Chaika, R. Tomala, W. Strek, Surface related laser induced white emission of Cr: YAG ceramic, Sci. Rep. 11 (2021) 14063–14067.
[27] M. Chaika, R. Lisiecki, K. Lesniewska-Matys, O.M. Vovk, A new approach for measurement of Cr^{4+} concentration in Cr^{4+}:YAG transparent materials: some conceptual difficulties and possible solutions, Opt. Mater. 126 (2022) 112126–112131.
[28] WANG S, YANG J, LI Y Q, et al. The improved size distribution and NIR luminescence of ZGGO: Cr^{3+} nanoparticles in-duced by Y^{3+} doping [J]. Mater. Res. Bull., 2024,169:112507.
[29] SUN X Y, DING N, HUANG W T, et al. Double perovskite $(Gd_{0.85-x}Y_x)_2MgTiO_6$: $0.3Eu^{3+}$ red phosphors for white LEDs with excellent high temperature performance [J]. Ceram. Int.,2019,45(16):20837-20843.